

### Inclusive spectra of charged hadrons from $\psi$ and $\psi'$ decays

D. G. Aschman, D. G. Coyne, D. E. Groom,\* G. K. O'Neill, H. F. W. Sadrozinski, and K. A. Shinsky†  
*Princeton University, Princeton, New Jersey 08540*

M. Cavalli-Sforza,‡ G. Goggi, F. Impellizzeri,§ M. Livan, F. Pastore, and B. Rossini¶  
*Istituto di Fisica Nucleare dell'Universita, Pavia, Italy*  
*and Istituto Nazionale di Fisica Nucleare, Sezione di Pavia, Italy*

D. H. Badtke,‡ B. A. Barnett,‡ L. H. Jones,§ and G. T. Zorn  
*University of Maryland, College Park, Maryland 20742*

L. P. Keller

*Stanford Linear Accelerator Center, Stanford, California 94305*

(Received 1 December 1980)

The inclusive charged-hadron momentum spectra from the  $\psi$  and  $\psi'$  decays produced in  $e^+e^-$  collisions at SPEAR are presented. The data were obtained with a small solid-angle, single-arm magnetic spectrometer with good particle-identification abilities centered at 90 degrees with respect to the beams. The particle-separated invariant cross sections are compared with data from  $e^+e^-$  collisions at  $\sqrt{s} = 4.8$  and 7.3 GeV, obtained with the same spectrometer, in order to observe the difference between hadron production at the resonances and in the continuum.

#### INTRODUCTION AND APPARATUS

Both psion production and nonresonant hadron production in  $e^+e^-$  annihilation take place through the one-photon channel; but while away from resonance hadrons are produced predominantly through the two-quark decays of the virtual photon, most of the hadron decays of the  $\psi$  are thought to proceed through gluons.<sup>1</sup> It is interesting to compare hadron spectra at the  $\psi$  and  $\psi'$  with hadron spectra at nonresonant energies. In this paper we shall present inclusive charged-hadron spectra for the decay of  $\psi(3095)$  and  $\psi'(3684)$  produced in  $e^+e^-$  collisions, obtained with the Maryland-Pavia-Princeton spectrometer at SPEAR. We shall compare these results to spectra obtained with the same spectrometer at  $\sqrt{s} = 4.8$  and 7.3 GeV.<sup>2,3</sup>

The experimental apparatus is shown in Figs. 1(a) and 1(b). It consisted of a magnetic spectrometer complemented by a central detector surrounding the interaction region, shower counters, and hadron filters. The main characteristics of the spectrometer are the following.

(1) Separation of hadrons from leptons using back-to-back shower counters and hadron filters.

(2) Hadron identification using a combination of a propane-filled threshold Čerenkov counter and of a time-of-flight system.

(3) A large magnetic-field integral permitting good momentum resolution.

The shower counter behind the magnet contained 7 radiation lengths of lead sandwiched with five layers of scintillator, each divided vertically into four counters, while the counter on the opposite

side of the interaction region consisted of 10 radiation lengths of sodium iodide supplemented by 7 radiation lengths of lead-scintillator sandwich. Located behind each shower counter was a hadron

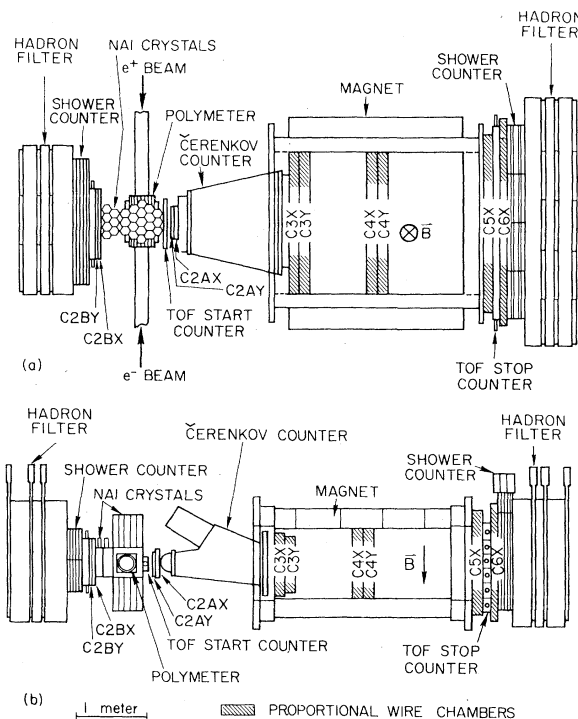


FIG. 1. Plan view (a) and side view (b) of the spectrometer used in this experiment.

filter composed of 6.8 collision lengths of iron interleaved with three layers of scintillation counters.

The time-of-flight system had a small start counter near the interaction region and a wall of seven stop counters arranged horizontally behind the magnet in front of the shower counters. All the time-of-flight counters were viewed by fast photomultiplier tubes (RCA8575) at both ends. The average flight path for a 1-GeV/c particle was 4.7 m. The system had a rms time resolution of 0.27 ns for muons.

The pressurized Čerenkov counter (90 psig of propane) was located immediately in front of the magnet and provided a signal for pions with momenta above 1.10 GeV/c and kaons with momenta above 3.70 GeV/c.

The central detector consisted of a cylindrical array of proportional tube counters, known as the polymeter, and four sets of proportional wire chambers surrounding it. The polymeter measured the azimuthal angle of particles emerging from the interaction point to  $\pm 3^\circ$ . The proportional chambers measured the polar angle over a limited solid angle of  $0.34 \times 4\pi$  sr.

Tracking and momentum measurements in the spectrometer used eight chambers before, inside, and after the magnet. Five of these measured the horizontal coordinate  $X$  and three measured the vertical coordinate  $Y$  of the charged-particle trajectories. The farthest chamber from the interaction point,  $C6X$ , consisted of proportional tubes.

Two chambers on the opposite side of the beams from the magnet measured the  $X$  and  $Y$  coordinates in front of the lead-scintillator shower counter.

All planar wire chambers had wire spacings of 2 mm. The sense wires in all chambers were 20- $\mu$ m gold-plated tungsten. The polymeter tubes had a diameter of 9.5 mm, while the last chamber behind the magnet had tubes of 19 mm diameter.

The magnet deflected charged particles in the horizontal plane, and was operated at a field integral of 0.79 Tm; for the 4.8- and 7.3-GeV data, the field integral was 1.18 Tm. For charged-particle momenta above 0.25 GeV/c, a resolution ( $\delta p/p$ ) =  $0.012 \times p$  ( $p$  in GeV/c) from measurement uncertainties, with an additional 0.003 arising from multiple scattering, was obtained. The solid angle subtended by the spectrometer at the interaction point was 0.094 sr.

Two additional stacks of sodium iodide crystals,<sup>4</sup> above and below the interaction region, are shown in Fig. 1 but were not used in the analysis of the data presented in this paper.

#### TRIGGERING, DATA ACQUISITION, AND DATA REDUCTION

The apparatus was triggered by the following conditions in coincidence: (1) Signals from the start and stop time-of-flight counters, (2) signals from at least two of the proportional chambers inside the magnet, and (3) a signal from the beam monitor, in time with the beam's crossing. Thus, a single-particle trigger necessary for the measurement of inclusive cross sections was attained. The trigger rate was typically a few per minute.

The data were taken at the peaks of the  $\psi$  or  $\psi'$  excitation curves. Two on-line minicomputers, an HP2114 and HP2100, operating in tandem, read in the data from each event, wrote it to magnetic tape, and provided on-line displays and diagnostics of chamber and apparatus performance.

Data reduction involved a selection stage to filter out nonreconstructable events, track finding in the chambers before the magnet, and trajectory fitting within the magnet. To eliminate backgrounds, fiducial cuts on the origin of the event were imposed. Tracks were required to be within  $\pm 7$  cm along the beam axis and within  $\pm 2$  cm vertically, based on the observed size of the luminous region.

#### PARTICLE IDENTIFICATION

For some of the events, the particle in the spectrometer could be readily identified. For instance, a collinear muon or electron pair would be promptly separated from the initial sample; likewise, a low-momentum ( $p < 1$  GeV/c) track associated with  $> 2$  charged particles and not triggering the Čerenkov counter would be labeled as a hadron. The time of flight would then identify it as a pion, kaon, or proton. Such clearly identified samples of spectrometer tracks were used to study the response of the particle-identification devices as a function of momentum and to define the probability that a muon, electron, or hadron of given momentum produce a given signal in the Čerenkov counter, the shower counters, or the muon filters.

Using these probability distributions, a muon, electron, or hadron label was assigned to each spectrometer track depending on which particle type would have the greatest probability of giving the observed response in the particle-identification devices. The overlaps of these probability distributions were used to estimate the contaminations in each final-particle sample. Analogous probability distributions, defined in terms of the time-of-flight values and Čerenkov amplitudes, were used to separate hadrons into pions, kaons, and antiprotons.

The detailed signatures required for identifica-

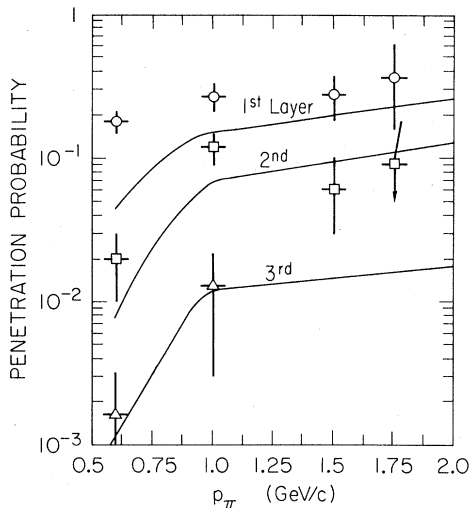


FIG. 2. Penetration probability of pions in the hadron filter. The solid lines are calculated from the data of Sander (Ref. 5), while the data points are the measured probabilities of penetrating the three layers of the hadron filter, obtained from a clean sample of pions from  $\psi'$  decays.

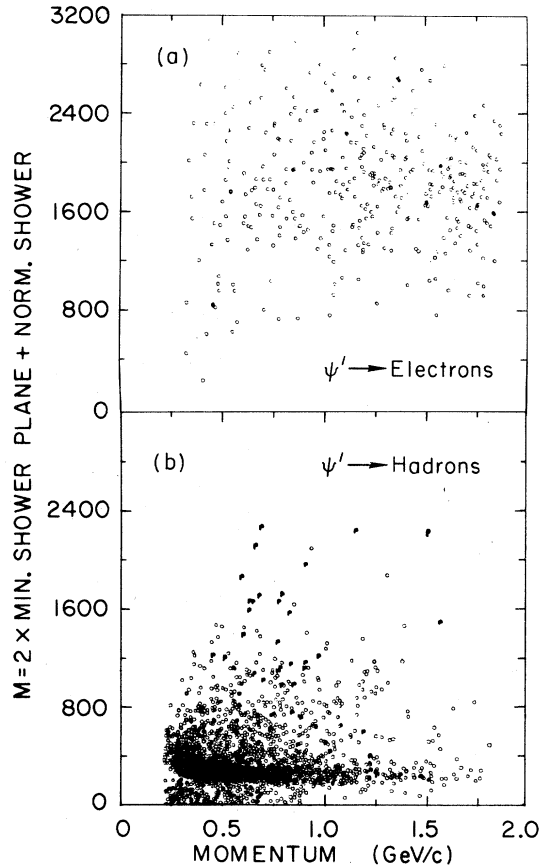


FIG. 3. Correlation plots between the quantity  $M$  defined in the text and momentum for the final sample of (a) electrons and (b) hadrons from the  $\psi'$  data. Hadrons labeled  $P$  are recognized as protons (antiprotons) by time of flight.

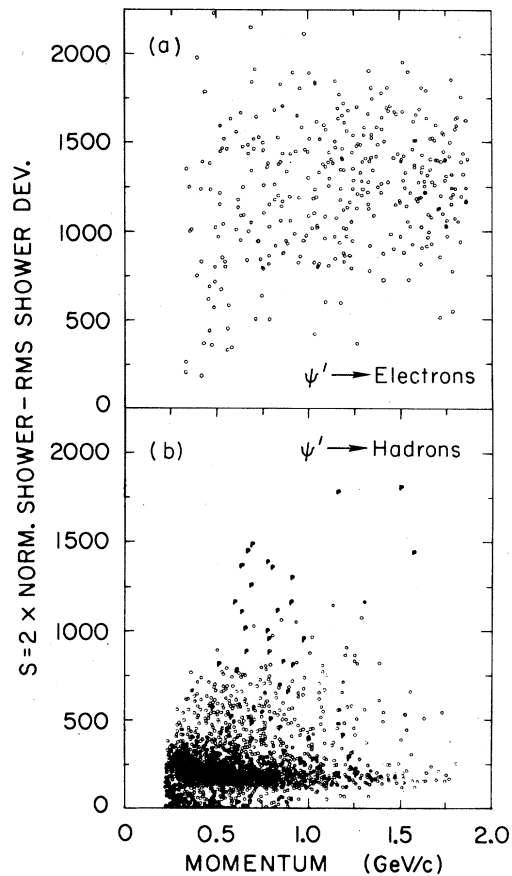


FIG. 4. Correlation plots between the quantity  $S$  defined in the text and momentum for the final sample of (a) electrons and (b) hadrons from the  $\psi'$  data. Hadrons labeled  $P$  are recognized as protons (antiprotons) by time of flight.

tion of each particle type are illustrated next.

Muons were identified by requiring a signal from the Čerenkov counter, a minimum amount of ionization in the shower counters, and penetration of at least the first two layers of the hadron filter by the track exiting from the magnet. This requirement limited the momentum of identifiable muons to  $p > 0.8$  GeV/ $c$ . Contamination of the muon sample by pions due to both penetration and decay was studied using a clean sample of pions from  $\psi'$  decays, and observing their probability to penetrate the three layers of the hadron filter. Figure 2 shows the results obtained and compares them to the measurements of Sander.<sup>5</sup> Above 0.8 GeV/ $c$ , the two sets of measurements agree.

Electrons were separated from hadrons on the basis of the Čerenkov signal for momenta below the pion threshold of 1.10 GeV/ $c$ , the shower-counter pulse height, and, in the case of electron pairs, the pulse height in the sodium iodide crys-

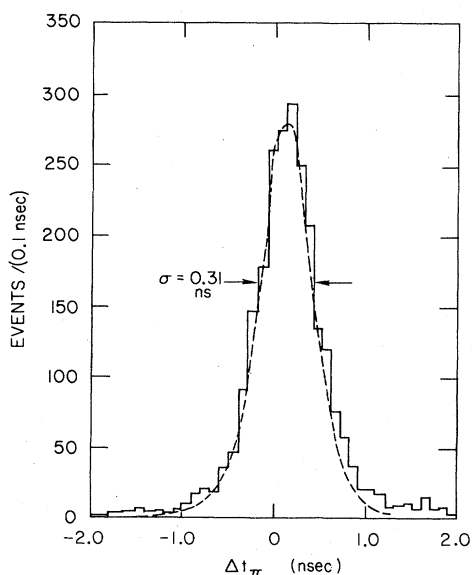


FIG. 5. The difference between the expected and the measured flight time for pions from the  $\psi'$ . The broken line is a Gaussian fit to the distribution with  $\sigma = 0.31 \pm 0.02$  nsec.

tals on the opposite side. Total shower-counter pulse-height information alone was not sufficient to separate electrons from hadrons. Two quantities derived from the pulse-height distribution within the shower counter were found to improve the electron-hadron separation. These were (a) the sum  $M = 2A_m + A_t$ , where  $A_m$  is the minimum pulse height of the first three shower-counter layers, and  $A_t$  is the total pulse height in the shower counter, and (b) the difference  $S = 2A_t - \sigma$  where  $\sigma$  is the rms deviation of the pulse heights

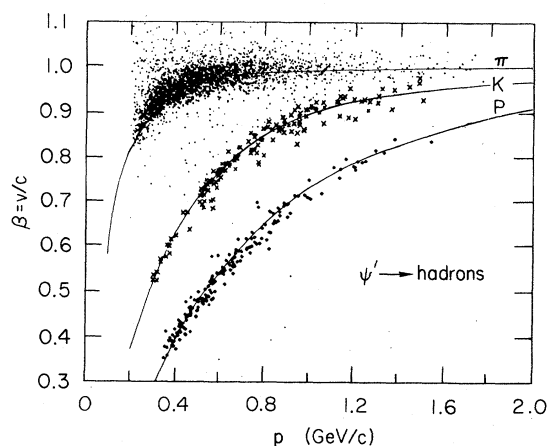


FIG. 6. Distribution of the observed velocity  $\beta$  for hadrons from the  $\psi'$  data set. The solid lines show  $\beta$  as a function of momentum for pions, kaons, and protons. The symbol  $\times$  indicates events within  $2\sigma$  of the kaons' expected flight time, while the symbol  $\blacklozenge$  indicates events within  $2\sigma$  of the protons' flight time.

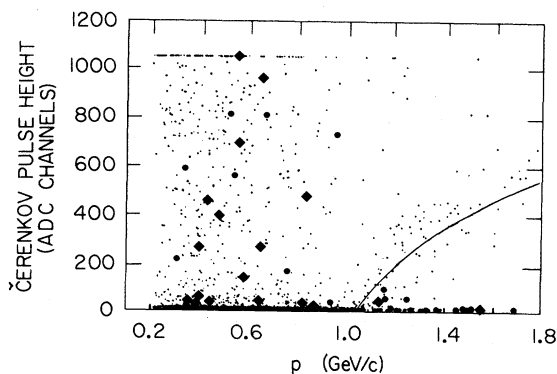


FIG. 7. The amplitude of the Čerenkov-counter signal for hadrons at the  $\psi'$ . The symbol  $\bullet$  indicates events within  $2\sigma$  of the kaons' expected flight time, while the symbol  $\blacklozenge$  indicates events within  $2\sigma$  of the protons' flight time. The solid line indicates the expected behavior for pions.

in the five shower-counter layers from their mean. Scatter plots of  $M$  and  $S$  against particle momenta are shown in Figs. 3 and 4 for the final electron and hadron samples. Some of the overlap in these distributions is due to protons and antiprotons that are clearly recognized on the basis of time of flight alone. Use of the Čerenkov-counter information removed most of the remaining ambiguity.

The worst-case remaining contamination of hadrons by electron occurs for momenta below  $0.7$  GeV/c and is  $(7 \pm 3) \times 10^{-4}$ ; this contamination in general is small because there are about ten times fewer electrons than hadrons in the spectrometer both at the  $\psi$  and the  $\psi'$ .

For momenta below  $1.10$  GeV/c the different hadronic species were identified by time of flight alone. Figure 5 shows the difference between the measured and expected time of flight for pions from the  $\psi'$ . In Fig. 6 the velocity  $\beta$  for all hadrons is plotted against the momentum. A clear separation between pions and kaons is evident for momenta below  $1.20$  GeV/c. Protons are clearly identified over the entire kinematic range.

To eliminate events from pion and kaon decay, the flight time for every identified particle was required to be within  $2\sigma$  of the value calculated from momentum for the most likely mass assignment.

The Čerenkov counter was used to separate pions from kaons and protons only for momenta  $p > 1.10$  GeV/c, the pion threshold momentum. Figure 7 shows the Čerenkov pulse height as a function of the measured hadron momentum. The pion signal shows the expected behavior above  $1.10$  GeV/c; below  $1.10$  GeV/c, however, 15% of the events show a spurious Čerenkov signal. Most of this background can be attributed to photons from the

decay of particles that convert in the materials preceding the Čerenkov radiator.

Contamination of kaons by the more numerous pion sample is only significant for  $1.0 < p < 1.10$  GeV/c, where time-of-flight information alone is used for hadron identification. In this momentum region, 0.2% of the kaons are estimated to be misidentified pions. Above the Čerenkov threshold, time-of-flight information limits the loss of kaons due to spurious Čerenkov signals to 3%, resulting in a 1.4% contamination of the pion sample by kaons for  $p > 1.10$  GeV/c.

Finally, the  $\psi$  data sample yielded 2210 pions, 111 kaons, and 133 protons and antiprotons. The  $\psi'$  sample yielded 2370 pions, 128 kaons, and 187 protons.

#### CORRECTION FACTORS AND CROSS-SECTION NORMALIZATION

The particle-separated spectra were then corrected for momentum-dependent effects. Corrections become prohibitively large for pions, kaons, and protons or antiprotons with momenta below 0.25, 0.4, and 0.5 GeV/c, respectively; cross sections could only be reliably calculated above these limits.

A detailed Monte Carlo calculation was used to simulate the traversal of particles through the spectrometer. Effects such as interactions in the detectors, particle decays, and reconstruction of decayed particles were considered. The momentum-dependent correction factors to be applied to the raw momentum spectra in order

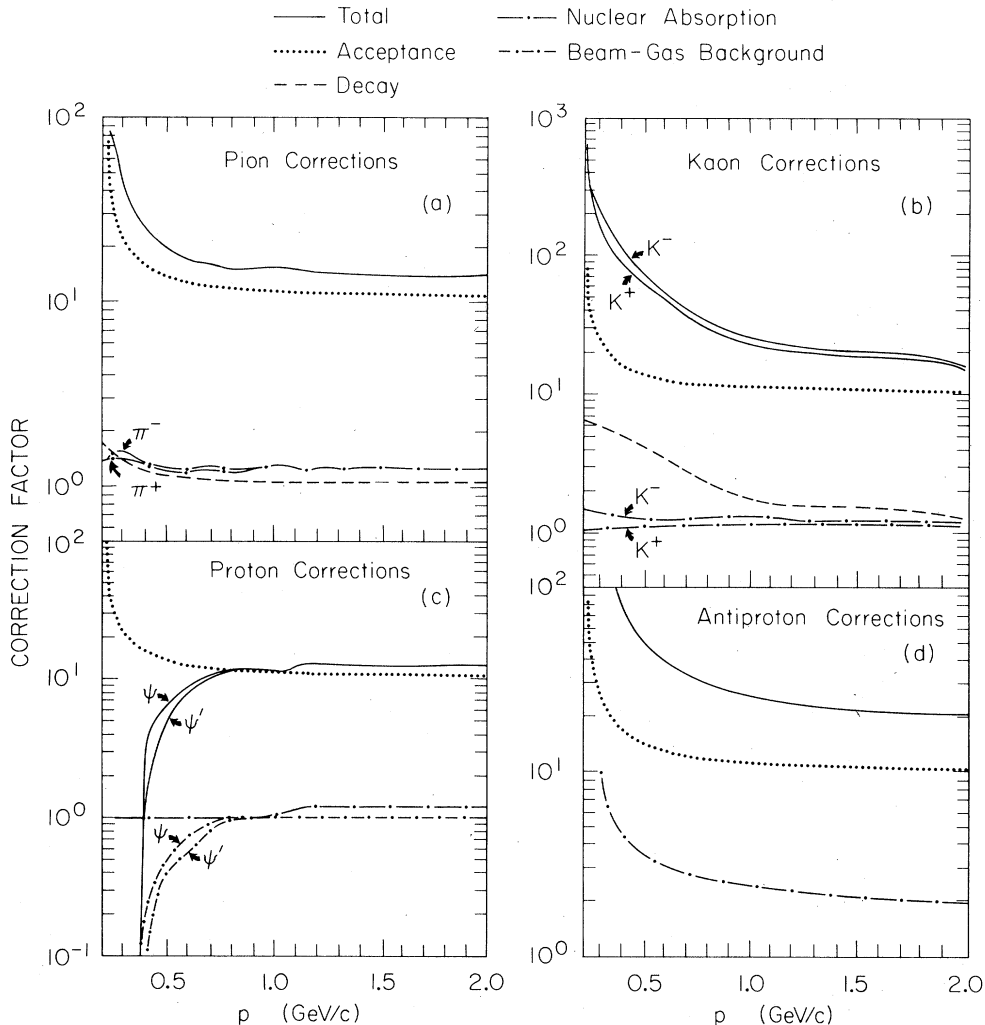


FIG. 8. Summary of the multiplicative correction factors that are applied to the observed (a) pion, (b) kaon, (c) proton, and (d) antiproton spectra to obtain the differential cross sections per steradian.

to obtain the number of particles per steradian are summarized in Figs. 8(a)–8(d) for pions, kaons, protons, and antiprotons separately. The individual effects considered were the following.

(a) *Momentum acceptance.* Due to the bending of charged-particle trajectories in the magnet, only 28% of the 0.094-sr solid angle of the spectrometer is accessible to particles with momenta  $p < 0.25$  GeV/c; this fraction rises to 85% for a 0.6-GeV/c particle.

(b) *Nuclear absorption.* The materials preceding the magnet were 0.21 nuclear collision lengths thick. Inelastic nuclear interactions in this part of the detector would either remove the particle entirely or produce secondaries that would not traverse the magnet, as verified by Monte Carlo calculations. The correction factors were calculated using, for each particle type, measured cross sections in Al, Fe, C, and H.<sup>6,7</sup> The factor for pions ranged from 1.5 to 1.25 for momenta between 0.25 and 1.5 GeV/c, and from 1.28 to 1.10 for kaons with momenta between 0.4 and 1.50 GeV/c. The correction factor for antiprotons exhibited the biggest momentum dependence, varying from 3.5 to 2.0 for momenta between 0.5 and 1.50 GeV/c.

(c) *Decays in flight.* Monte Carlo-generated decays of pions and kaons in the spectrometer

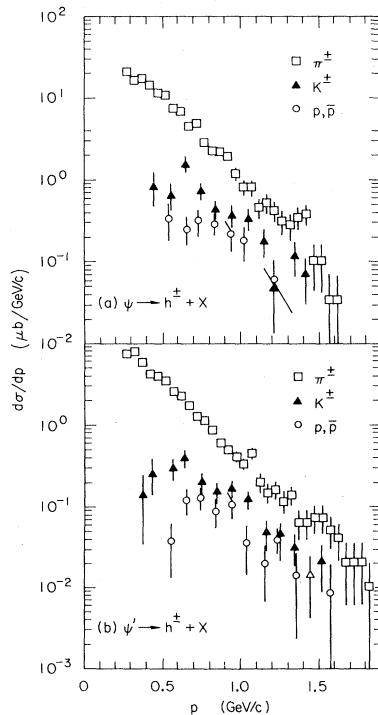


FIG. 9. Inclusive momentum spectra integrated over the solid angle for  $\pi^\pm$ ,  $K^\pm$ ,  $p$ ,  $\bar{p}$  at the  $\psi$  and  $\psi'$ .

TABLE I. The inclusive sections  $d\sigma/dp$  as functions of hadron momentum for charged pions and kaons, and for protons (or antiprotons) produced at the  $\psi$ . The values of momentum quoted correspond to the center of each bin. The notation  $0+\dots$  indicates a 1-standard-deviation upper limit.

$p$ (GeV/c)	$d\sigma/dp$ [( $\mu\text{b}/\text{GeV}/c$ )]	$p$ (GeV/c)	$d\sigma/dp$ [( $\mu\text{b}/\text{GeV}/c$ )]
	$\pi^\pm$		$K^\pm$
0.275	20.5 $\pm$ 2.3	0.45	0.85 $\pm$ 0.37
0.325	16.5 $\pm$ 1.4	0.55	0.66 $\pm$ 0.24
0.375	16.8 $\pm$ 1.1	0.65	1.56 $\pm$ 0.30
0.425	14.5 $\pm$ 1.0	0.75	0.75 $\pm$ 0.18
0.475	11.5 $\pm$ 0.8	0.85	0.44 $\pm$ 0.13
0.525	10.5 $\pm$ 0.7	0.95	0.38 $\pm$ 0.11
0.575	7.67 $\pm$ 0.58	1.05	0.35 $\pm$ 0.10
0.625	6.96 $\pm$ 0.54	1.15	0.18 $\pm$ 0.07
0.675	4.55 $\pm$ 0.43	1.25	0.050 $\pm$ 0.035
0.725	5.04 $\pm$ 0.44	1.35	0.12 $\pm$ 0.06
0.775	2.90 $\pm$ 0.33	1.45	0.072 $\pm$ 0.04
0.825	2.30 $\pm$ 0.29		
0.875	2.23 $\pm$ 0.29		$p, \bar{p}$
0.925	1.95 $\pm$ 0.27	0.45	0.019 $\pm$ 0.015
0.975	1.19 $\pm$ 0.21	0.55	0.34 $\pm$ 0.16
1.025	0.83 $\pm$ 0.18	0.65	0.26 $\pm$ 0.10
1.075	0.81 $\pm$ 0.17	0.75	0.32 $\pm$ 0.11
1.125	0.47 $\pm$ 0.13	0.85	0.30 $\pm$ 0.09
1.175	0.53 $\pm$ 0.14	0.95	0.23 $\pm$ 0.09
1.225	0.43 $\pm$ 0.12	1.05	0.19 $\pm$ 0.09
1.275	0.32 $\pm$ 0.11	1.15	0 $\pm$ 0.05
1.325	0.28 $\pm$ 0.10	1.25	0.064 $\pm$ 0.043
1.375	0.36 $\pm$ 0.11		
1.425	0.39 $\pm$ 0.12		
1.475	0.11 $\pm$ 0.06		
1.525	0.11 $\pm$ 0.06		
1.575	0.035 $\pm$ 0.035		
1.625	0.034 $\pm$ 0.034		

were submitted to the reconstruction programs in order to determine what fraction of the particles would decay and not appear in the final event sample. This could occur due to failure of the decay products to trigger the apparatus, to be reconstructed, or to be identified as a hadron; for example, by the time-of-flight cut. At 0.5 GeV/c, typically 80% of the kaons and 15% of the pions were lost. The calculated correction factors are plotted in Figs. 8(a) and 8(b).

(d) *Particle misidentification.* Corrections were applied to each particle sample to account for cuts and losses due to the particle-identification procedure, and for the calculated contaminations from other particle types. The net result of these two effects on the hadron sample from separating electrons and muons is an overall loss of 0.3%, with only a slight momentum dependence. The worst-case contaminations and losses associated

with sorting hadrons into pions, kaons, and protons (antiprotons) have been indicated in the previous section. All spectra were corrected for the  $2\sigma$  fiducial cut on time of flight.

(e) *Machine-induced backgrounds.* Examination of events whose intercept with the beam axis was more than 10 cm away from the center of the interaction region allowed an estimation of the beam-gas background. For the pion, kaon, and anti-proton sample this was found to be less than 0.5% and was neglected. For proton a momentum-dependent correction was applied and is shown in Fig. 8(d).

(f) *Correction to momentum from energy losses.* The measured momentum was corrected for losses due to ionizing collisions while traversing material before the magnet. This correction is approximately +25 MeV/c for pions over the entire momentum range, but rises to +60 MeV/c for kaons with  $p = 0.4$  GeV/c and +92 MeV/c for protons with  $p = 0.5$  GeV/c.

The integrated luminosity for the  $\psi'$  and  $\psi$  data samples was calculated from the number of muon-pair events detected in the spectrometer. We obtained an integrated luminosity of  $106 \pm 10$  nb $^{-1}$  at the  $\psi$  and  $360 \pm 37$  nb $^{-1}$  at the  $\psi'$ . At the  $\psi'$ , the muons from the  $\psi$  decay were also used in order to reduce the statistical error, since the branching ratio for  $\psi' \rightarrow \psi + \text{anything}$  is measured.<sup>8,9</sup> The errors quoted reflect both statistical and branching fraction uncertainties.

## RESULTS AND DISCUSSION

The inclusive momentum spectra for pions, kaons, and protons and antiprotons from the decays of  $\psi$  and  $\psi'$  are shown in Fig. 9, and in Tables I and II. The errors shown include both the statistical and systematic uncertainties, but not the overall normalization uncertainty from the luminosity measurement. Differential cross sections observed in the spectrometer were integrated over the entire solid angle, assuming an isotropic distribution of hadrons. The spectra for both particle and antiparticle, including protons and antiprotons, were the same within statistics.

The spectra have a smooth falloff with momentum, except for one notable enhancement in the pion spectrum from the  $\psi$  at a momentum of 1.40 GeV/c. This corresponds to the two-body decay  $\psi \rightarrow \pi^+\rho$  with the pion recoiling into the spectrometer. From this enhancement and assuming a  $1 + \cos^2\theta$  distribution, we measure a branching ratio

$$B(\psi \rightarrow \pi^+\rho) = 0.007 \pm 0.003$$

in good agreement with previous results.<sup>9</sup>

Figure 10 gives the invariant cross sections

TABLE II. The inclusive cross sections  $d\sigma/dp$  as functions of hadron momentum for charged pions and kaons, and for protons (or antiprotons) produced at the  $\psi'$ . See Table I for notation.

$p$ (GeV/c)	$d\sigma/dp$ [( $\mu\text{b}/(\text{GeV}/c)$ )]	$p$ (GeV/c)	$d\sigma/dp$ [( $\mu\text{b}/(\text{GeV}/c)$ )]
	$\pi^\pm$		$K^\pm$
0.275	$7.39 \pm 0.79$	0.45	$0.26 \pm 0.12$
0.325	$7.84 \pm 0.52$	0.55	$0.29 \pm 0.09$
0.375	$5.77 \pm 0.37$	0.65	$0.38 \pm 0.08$
0.425	$4.18 \pm 0.28$	0.75	$0.19 \pm 0.05$
0.475	$3.96 \pm 0.25$	0.85	$0.15 \pm 0.04$
0.525	$3.45 \pm 0.22$	0.95	$0.16 \pm 0.04$
0.575	$2.56 \pm 0.18$	1.05	$0.12 \pm 0.03$
0.625	$2.29 \pm 0.17$	1.15	$0.048 \pm 0.020$
0.675	$1.73 \pm 0.14$	1.25	$0.045 \pm 0.018$
0.725	$1.25 \pm 0.12$	1.35	$0.030 \pm 0.015$
0.775	$1.12 \pm 0.11$	1.45	$0.014 \pm 0.010$
0.825	$0.88 \pm 0.10$	1.55	$0.021 \pm 0.012$
0.875	$0.59 \pm 0.08$		
0.925	$0.50 \pm 0.07$		
0.975	$0.41 \pm 0.07$		
1.025	$0.33 \pm 0.06$	0.45	$0.008 \pm 0.004$
1.075	$0.44 \pm 0.07$	0.55	$0.037 \pm 0.024$
1.125	$0.19 \pm 0.05$	0.65	$0.12 \pm 0.04$
1.175	$0.15 \pm 0.04$	0.75	$0.13 \pm 0.04$
1.225	$0.16 \pm 0.04$	0.85	$0.087 \pm 0.035$
1.275	$0.12 \pm 0.035$	0.95	$0.105 \pm 0.035$
1.325	$0.14 \pm 0.04$	1.05	$0.035 \pm 0.022$
1.375	$0.064 \pm 0.026$	1.15	$0.020 \pm 0.013$
1.425	$0.064 \pm 0.026$	1.25	$0.038 \pm 0.018$
1.475	$0.075 \pm 0.028$	1.35	$0.014 \pm 0.011$
1.525	$0.074 \pm 0.028$	1.45	$0 \pm 0.01$
1.575	$0.052 \pm 0.023$	1.55	$0.009 \pm 0.010$
1.625	$0.042 \pm 0.021$		
1.675	$0.021 \pm 0.015$		
1.725	$0.021 \pm 0.015$		
1.775	$0.021 \pm 0.015$		
1.825	$0.010 \pm 0.010$		

as a function of the particle momentum. The data are well described by the simple exponential form of the type  $A \exp(-Bp)$ . The fitted parameters  $A$  and  $B$  are given in Table III. The slopes  $B$  for the  $\psi$  and  $\psi'$  are the same within errors; while this must reflect the well-known fact that more than half of the  $\psi'$  decays proceed through the  $\psi$  (in turn decaying almost at rest), it is also an indication that the  $\psi'$  decays which do not involve the  $\psi$  are not much different from  $\psi$  decays. Our lower momentum cut of 0.25 GeV/c for the pion momentum precludes the observation of most of the slow pions from the process  $\psi' \rightarrow \pi^+\pi^-\psi$ .

Given the observed exponential behavior of the invariant cross sections versus momentum, it is of some interest to compare to each other the three-particle cross sections as a function of the

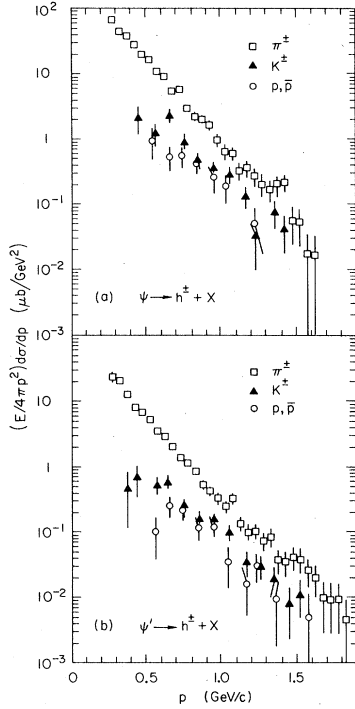


FIG. 10. The particle-separated invariant cross sections at the  $\psi$  and the  $\psi'$  as a function of hadron momentum.

particle energy at the  $\psi$  (and  $\psi'$ ). Thermodynamical models for hadron production<sup>10</sup> provide one scheme for exponentially decreasing total energy spectra; if the production process is totally insensitive to hadron identity, one might expect both magnitude and slope of the invariant cross sections to be the same. Figure 11 and Tables IV and V show the invariant cross sections for each particle type at the  $\psi$  and  $\psi'$ , as a function of the particle energy. Each particle spectrum was fitted to an exponential shape and the results are shown in Table VI. Whereas the slopes of the three-particle cross sections are independent (within the errors) of particle type, the magnitudes are not; the proton cross section is higher than that for pions; the kaon cross section is lower. Not surprisingly in light of the previous results, no difference in the slopes of the three-particle cross sections versus energy at the  $\psi$  and  $\psi'$  is apparent.

The charged-hadron spectra from the  $\psi$  and  $\psi'$  decays have also been measured by the DASP collaboration at DORIS<sup>11</sup>; their results, however, were obtained integrating the momentum spectra over the entire width of the resonances. In order to compare the two sets of results, the DASP spectra were divided by the ratio between the

TABLE III. Exponential fits to the invariant cross sections as a function of momentum at the  $\psi$  and the  $\psi'$  in the form  $(E/4\pi p^2)d\sigma/dp = Ae^{-Bp}$ . The  $\psi'$  results are only fitted for  $p > 0.4$  GeV/c to eliminate the slow pions from the decay  $\psi' \rightarrow \pi^+ \pi^- \psi$ .

Particle	A ( $\mu\text{b}/\text{GeV}^2$ )	B (c/GeV)	$\chi^2/\text{DOF}$
$\psi$ decays			
$\pi^\pm$	$37.56 \pm 0.15$	$6.02 \pm 0.18$	16.9/14
$K^\pm$	$4.52 \pm 0.11$	$5.03 \pm 0.06$	14.5/6
$p, \bar{p}$	$0.52 \pm 0.01$	$3.11 \pm 0.20$	0.56/5
$\psi'$ decays $p > 0.4$ GeV/c			
$\pi^\pm$	$10.8 \pm 0.1$	$5.83 \pm 0.17$	14.1/14
$K^\pm$	$0.78 \pm 0.06$	$4.34 \pm 0.42$	4.64/6
$p, \bar{p}$	$0.23 \pm 0.02$	$3.50 \pm 0.84$	19.1/6

area under the resonance curves and the resonance area spanned by our experiment, at the peak of the resonances, due to the machine width. These scale factors are 4.7 at the  $\psi$  and 6.1 at the  $\psi'$  and were obtained using the SLAC-LBL values for the area under the resonances and for the total hadronic cross sections at the  $\psi$  and  $\psi'$  peaks.<sup>12</sup> A comparison of the two sets of results is shown in Fig. 12. The agreement between the two experiments is excellent for the pion and kaon spectra, while the proton spectra show some dif-

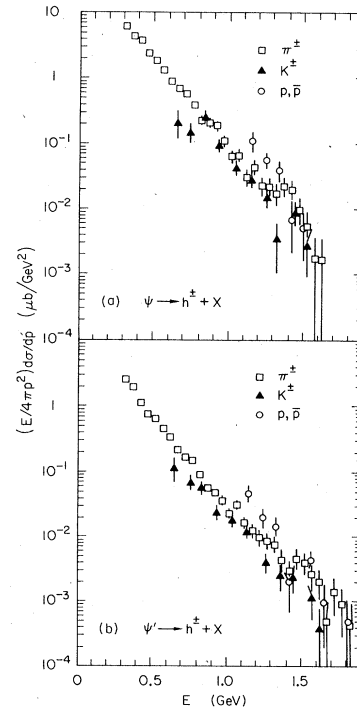


FIG. 11. The particle-separated invariant cross sections at the  $\psi$  and the  $\psi'$  as a function of hadron energy.



TABLE IV. The invariant cross sections  $(E/4\pi p^2)d\sigma/dp$  as a function of the hadron total energy  $E$  for charged pions and kaons and for protons (or antiprotons) at the  $\psi$ . The energies are given for the center of each bin.

$E$ (GeV)	$(E/4\pi p^2)d\sigma/dp$ [(nb/(GeV <sup>2</sup> ))]	$E$ (GeV)	$(E/4\pi p^2)d\sigma/dp$ [(nb/(GeV <sup>2</sup> ))]
	$\pi^\pm$		$K^\pm$
0.325	6255 ± 562	0.65	217 ± 97
0.375	4386 ± 322	0.75	155 ± 50
0.425	3670 ± 231	0.85	243 ± 45
0.475	2388 ± 158	0.95	94.4 ± 21.0
0.525	1876 ± 124	1.05	43.9 ± 11.9
0.575	1358 ± 96	1.15	29.7 ± 8.6
0.625	897 ± 71	1.25	15.9 ± 5.7
0.675	698 ± 59	1.35	7.0 ± 2.5
0.725	597 ± 52	1.45	9.2 ± 3.8
0.775	381 ± 39	1.55	5.7 ± 2.0
0.825	226 ± 29		$p, \bar{p}$
0.875	211 ± 27		
0.925	191 ± 25	1.05	175 ± 48
0.975	112 ± 19	1.15	114 ± 29
1.025	65.7 ± 14.0	1.25	56.8 ± 14.1
1.075	67.5 ± 13.8	1.35	39.2 ± 13.6
1.125	31.4 ± 9.1	1.45	13.8 ± 4.8
1.175	43.4 ± 10.4	1.55	10.6 ± 3.5
1.225	23.4 ± 7.4		
1.275	22.3 ± 7.1		
1.325	17.4 ± 6.2		
1.375	23.0 ± 6.9		
1.425	20.1 ± 6.3		
1.475	9.7 ± 4.3		
1.525	5.5 ± 3.2		
1.575	1.8 ± 1.8		
1.625	1.7 ± 1.7		

ferences in both shape and magnitude.

We turn now to a comparison with inclusive hadron spectra at nonresonant energies. We have accordingly normalized the cross sections at different center-of-mass energies to the integral of the invariant cross section, which is the product of the average charged-particle energy and the total cross section. Values for these two latter quantities are taken from Ref. 12. Figure 13 shows a comparison of the pion and kaon cross sections at the  $\psi$  and  $\psi'$  with the nonresonant data at energies of 4.8 and 7.3 GeV obtained with the same spectrometer.<sup>2,3</sup> The nonresonant data deviate from exponential behavior; this deviation is greatest for the 7.3-GeV data, where a  $p^{-4}$  dependence fitted the data better than an exponential, as expected from various scaling models.<sup>13</sup> On the basis of our data alone, it is not possible to decide whether the differences between the three energies depend on the annihilation proceeding through a resonant state, or are simply due to the effect of lower center-of-mass energy. A similar comparison has been made by the DASP

TABLE V. The invariant cross sections  $(E/4\pi p^2)d\sigma/dp$  as a function of the hadron total energy  $E$  for charged pions and kaons and for protons (or antiprotons) at the  $\psi'$ . The energies are given for the center of each bin.

$E$ (GeV)	$(E/4\pi p^2)d\sigma/dp$ [(nb/(GeV <sup>2</sup> ))]	$E$ (GeV)	$(E/4\pi p^2)d\sigma/dp$ [(nb/(GeV <sup>2</sup> ))]
	$\pi^\pm$		$K^\pm$
0.325	2472 ± 194	0.65	116 ± 48
0.375	1911 ± 116	0.75	68.3 ± 17.3
0.425	1082 ± 69	0.85	56.5 ± 12.1
0.475	746 ± 49	0.95	24.2 ± 5.8
0.525	636 ± 40	1.05	18.5 ± 4.3
0.575	442 ± 30	1.15	12.6 ± 3.1
0.625	324 ± 23	1.25	4.1 ± 1.5
0.675	211 ± 18	1.35	2.5 ± 1.1
0.725	166 ± 15	1.45	2.3 ± 1.0
0.775	147 ± 13	1.55	2.3 ± 0.7
0.825	91.2 ± 10.0	1.65	0.76 ± 0.38
0.875	56.1 ± 7.6	1.75	0 ± 0.2
0.925	47.6 ± 6.8	1.85	0 ± 0.1
0.975	37.1 ± 5.9		$p, \bar{p}$
1.025	23.2 ± 4.6		
1.075	31.9 ± 5.2	1.15	45.6 ± 11.9
1.125	17.2 ± 3.7	1.25	20.1 ± 6.5
1.175	12.5 ± 3.0	1.35	14.7 ± 4.7
1.225	9.8 ± 2.6	1.45	4.0 ± 1.4
1.275	8.8 ± 2.4	1.55	4.3 ± 1.8
1.325	7.8 ± 2.2	1.65	1.0 ± 0.8
1.375	4.4 ± 1.6	1.75	0 ± 0.5
1.425	3.0 ± 1.3	1.85	1.0 ± 0.6
1.475	4.6 ± 1.6		
1.525	3.9 ± 1.5		
1.575	2.7 ± 1.2		
1.625	2.0 ± 1.0		
1.675	0.50 ± 0.50		
1.725	1.4 ± 0.8		
1.775	0.93 ± 0.66		
1.825	0.45 ± 0.45		

collaboration<sup>14</sup> using their particle separated spectra at  $\sqrt{s} = 3.6$  GeV and at the  $\psi$ . The DASP data exhibit a slight excess of high-energy hadrons in the  $\psi$  data over the nonresonant data, although the differences do not appear to be very significant.

We turn next to a discussion of the relative rate of the production of different hadron types, defined as the corrected number of  $K^\pm$ ,  $\pi^\pm$ , or  $p, \bar{p}$  divided by the sum of these hadrons. For the  $\psi$  and  $\psi'$  decays, the data are displayed as a function of momentum in Fig. 14. The charged-kaon fraction is observed to increase with momentum, reaching a value of approximately 0.25; protons and antiprotons together exhibit the same behavior with momentum, approaching a fraction of about 0.1 at the kinematic limit. Particle fractions versus momentum do not differ, within errors, at the  $\psi$  and  $\psi'$  over the observed momentum ranges.

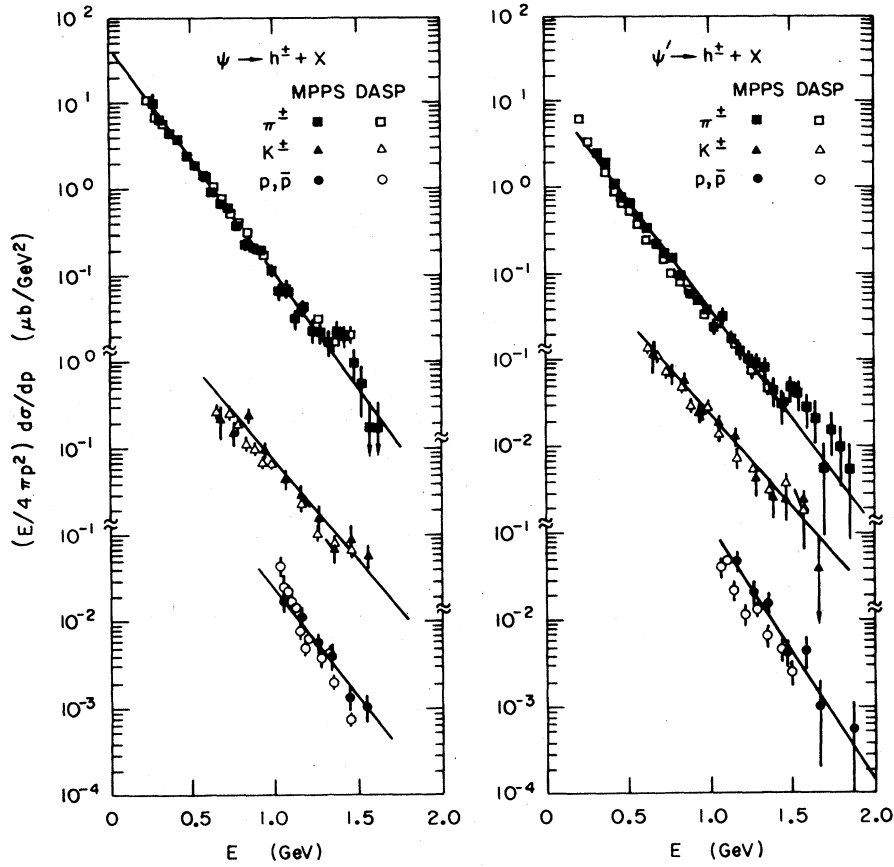


FIG. 12. Comparison of the particle-separated invariant cross sections at the  $\psi$  and the  $\psi'$  obtained by this experiment and by the DASP collaboration (Ref. 11). The latter results have been divided by scale factors of 4.7 at the  $\psi$  and 6.1 at the  $\psi'$  as described in the text.

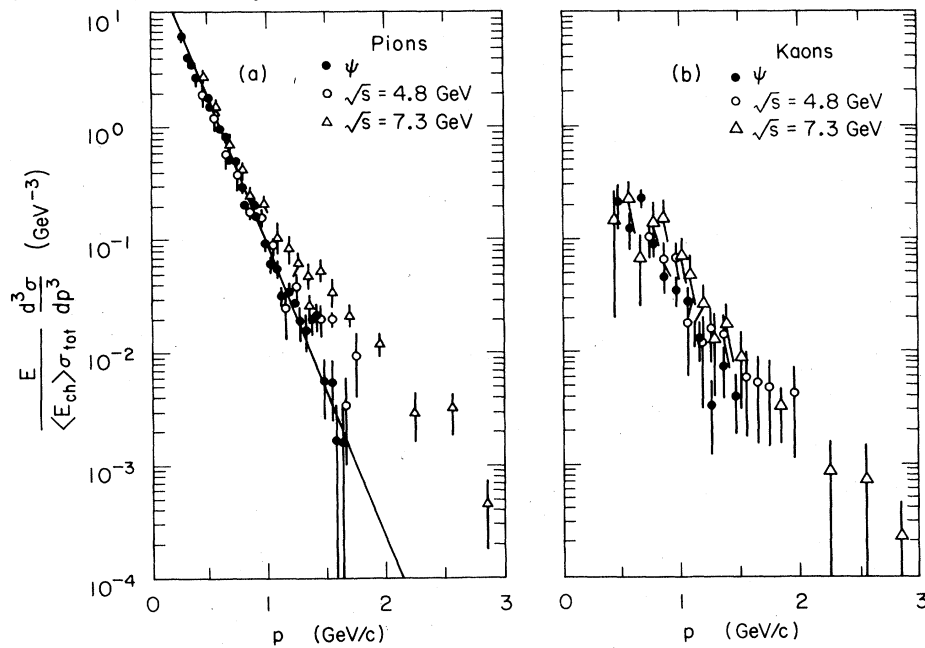


FIG. 13. Comparison of the invariant cross sections for (a) charged pions and (b) kaons at the  $\psi$ , at  $\sqrt{s}=4.8$  and 7.3 GeV. The line in part (a) is the fitted curve for the pions from the  $\psi$ . The cross sections are normalized by the integral of each cross section over momentum.

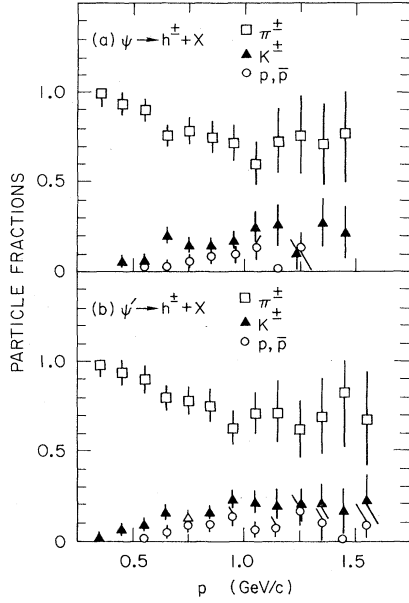


FIG. 14. The fraction of  $\pi^\pm$ ,  $K^\pm$ , and  $p, \bar{p}$  (a) from  $\psi$  decays and (b) from  $\psi'$  decays as a function of hadron momentum.

Figure 15 contains a comparison among kaon fractions from the  $\psi$  data and the data at  $\sqrt{s}=4.8$  and 7.3 GeV. Over the common momentum range, the fractions do not differ appreciably.

The overall fractions of each particle type, integrated over momentum, can be calculated assuming the exponential fits to the invariant particle cross sections in Table VI can be extrapolated to zero momentum. We then obtain the following

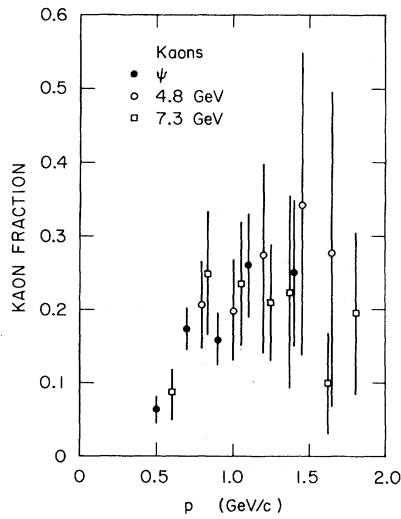


FIG. 15. Comparison of  $K^\pm$  fractions vs momentum at  $\psi$ , at  $\sqrt{s}=4.8$  and 7.3 GeV.

TABLE VI. Exponential fits to the invariant cross sections as a function of the hadrons total energy in the form  $(E/4\pi p^2)d\sigma/dp = A e^{-BE}$ . The  $\psi'$  results are only fitted for  $p > 0.4$  GeV/c (see Table III).

Particle	A ( $\mu\text{b}/\text{GeV}^2$ )	B ( $\text{GeV}^{-1}$ )	$\chi^2/\text{DOF}$
$\psi$ decays			
$\pi^\pm$	$45.1 \pm 0.1$	$6.13 \pm 0.17$	16.1/14
$K^\pm$	$13.8 \pm 0.2$	$5.29 \pm 0.89$	12.3/5
$p, \bar{p}$	$95.2 \pm 3.5$	$5.92 \pm 0.95$	1.28/4
$\psi'$ decays $E > 0.4$ GeV			
$\pi^\pm$	$13.8 \pm 0.2$	$6.00 \pm 0.17$	18.4/14
$K^\pm$	$3.45 \pm 0.05$	$5.06 \pm 0.4$	2.69/5
$p, \bar{p}$	$57.1 \pm 10.5$	$6.3 \pm 1.2$	7.7/6

fractions for the  $\psi$ :

$$F(\pi^\pm) = 0.88 \pm 0.01,$$

$$F(K^\pm) = 0.10 \pm 0.01,$$

$$F(p + \bar{p}) = 0.022 \pm 0.002,$$

and for the  $\psi'$ :

$$F(\pi^\pm) = 0.87 \pm 0.01,$$

$$F(K^\pm) = 0.10 \pm 0.01,$$

$$F(p + \bar{p}) = 0.023 \pm 0.002.$$

It is of some interest to find whether the *inclusive* particle fractions we measure are in agreement with the particle fractions that can be calculated from the measured exclusive decay channels, with some reasonable assumption on the undetected exclusive channels. This comparison is particularly interesting at the  $\psi$ , where although many exclusive decay modes have been measured only 63% of the hadronic decays can be accounted for on the basis of the reconstructed decay modes.<sup>8</sup> Differences between the measured inclusive fractions and the fraction calculated from measured decays would be indicative of the charged-particle composition of the unmeasured ones. In order to account for the unmeasured charge states of a given channel (for instance,  $\psi \rightarrow 2\pi^+2\pi^-3\pi^0$ , where only  $\psi \rightarrow 3\pi^+3\pi^-\pi^0$  has been measured) a statistical model was used in analogy to the procedure explained in the review paper by Feldman and Perl.<sup>8,15</sup> Weighting each state by its probability to be detected in the spectrometer (including the charged decays of  $K_S^0$ ,  $\eta$ , and  $\phi$ ) we calculate from the measured exclusive decays

$$F(\pi^\pm) = 0.89 \pm 0.01,$$

$$F(K^\pm) = 0.09 \pm .01,$$

$$F(p + \bar{p}) = 0.023 \pm .004.$$

The excellent agreement with our measurements indicates that the charged-particle composition of the undetected channels does not differ greatly from the composition of the measured decays.

#### ACKNOWLEDGMENTS

We would like to express our gratitude to M. Bowlby, B. Gibbs, G. Iuvino, R. Nardo, and W. Werosta for their expert and dedicated technical help. In particular, we appreciate the efforts of the late G. Magnani, who devoted a part of his life with great effort and enthusiasm

to this experiment. We also acknowledge the efforts of the SLAC and SPEAR operations groups, as well as the help we received from the SLAC Experimental Facilities Division, especially from B. Denton and E. Keyser. T. Gabriel from ORNL helped us to run his HETC code and to further our understanding of the detector. One of us (D.E.G.) thanks the Princeton group for their hospitality. This work was supported by the National Science Foundation under Contracts Nos. MPS 71-02657 and PHY 76-06642 by the Istituto Nazionale di Fisica Nucleare and the U. S. Energy Research and Development Administration.

\*Permanent address: Physics Department, University of Utah, Salt Lake City, Utah 84112.

†Present address: Department of Physics, University of California, Berkeley, California 94720.

‡Present address: Physics Department, Princeton University, Princeton, New Jersey 08544.

¶Present address: Realizzazioni Tecnologiche Avanzate, Via Folperti 44/B, 27100 Pavia, Italy.

‡Present address: Physics Department, Johns Hopkins University, Baltimore, Maryland 21218.

§Present address: Fairchild Camera and Instrument Co., Palo Alto, California 94300.

<sup>1</sup>See, for instance, T. Appelquist, R. M. Barnett, and K. D. Lane, *Annu. Rev. Nucl. Sci.* **28**, 387 (1978).

<sup>2</sup>T. L. Atwood *et al.*, *Phys. Rev. Lett.* **35**, 704 (1975).

<sup>3</sup>D. G. Aschman *et al.*, *Phys. Rev. Lett.* **41**, 445 (1978).

<sup>4</sup>C. Biddick *et al.*, *Phys. Rev. Lett.* **38**, 1324 (1977).

<sup>5</sup>H. G. Sander, Diplomarbeit, Aachen University, 1974 (unpublished).

<sup>6</sup>K. A. Shinsky, Ph.D. thesis, Princeton University, 1978 (unpublished); D. H. Badtke, Ph.D. thesis, University

of Maryland, 1978 (unpublished).

<sup>7</sup>High Energy Reactions Analysis Group, CERN Report No. 72-1, 1972 (unpublished); CERN Report No. 75-1, 1975 (unpublished); J. W. Cronin, R. Cool, and A. Abashian, *Phys. Rev.* **107**, 1121 (1957); R. L. Martin, *ibid.* **87**, 1052 (1954); M. J. Longo and B. J. Moyer, *ibid.* **125**, 701 (1962).

<sup>8</sup>G. J. Feldman and M. L. Perl, *Phys. Rep.* **33C**, 285 (1977).

<sup>9</sup>R. Brandelik *et al.*, *Z. Phys. C* **1**, 233 (1979).

<sup>10</sup>R. Hagedorn, *Nucl. Phys.* **B24**, 93 (1970); E. L. Feinberg, *Phys. Rep.* **5C**, 237 (1972).

<sup>11</sup>W. Braunschweig *et al.*, *Phys. Lett.* **63B**, 115 (1976).

<sup>12</sup>G. J. Feldman and M. L. Perl, *Phys. Rep.* **19C**, 233 (1975).

<sup>13</sup>S. M. Berman, J. D. Bjorken, and J. B. Kogut, *Phys. Rev. D* **4**, 3388 (1971); S. D. Drell, D. J. Levy, and T. M. Yan, *ibid.* **1**, 1617 (1970).

<sup>14</sup>R. Brandelik *et al.*, *Nucl. Phys.* **B148**, 189 (1979).

<sup>15</sup>A. Pais, *Phys. Rev. Lett.* **32**, 1081 (1974); *Ann. Phys. (N.Y.)* **9**, 548 (1960).